JOURNAL OF SPACECRAFT AND ROCKETS
Vol. 44, No. 4, July–August 2007

Sizing/Optimization of a Small Satellite Energy Storage and Attitude Control System

David J. Richie,* Vaios J. Lappas,† and Phil L. Palmer‡
University of Surrey, Guildford, GU2 7XH England, United Kingdom

DOI: 10.2514/1.25134

The recent advent of miniature single gimbal control moment gyroscopes has spawned interest in variable-speed versions for combined energy storage and attitude control systems on small satellites. Although much has been studied on the theory behind such a system, little has been done in optimally sizing these actuators for small satellite applications. This paper investigates optimally sizing these actuators for a practical space mission. Given a set of small satellite agility and energy storage requirements, the design is cast as a constrained nonlinear programming problem using a performance index constructed from subsystem design margins and solved using a reduced-order, gradient-based solver software code. By iterating this process for different input conditions and technologies, several design points were created, then scored using a weighted scoring function, and evaluated. The resulting method permits an efficient, structured approach to designing an optimally sized combined energy storage and attitude control system while enabling alternative technology comparisons.

Nomenclature

C	=	storage capacity, W · h
d_{ty}	=	eclipse duty cycle, %
E	=	modulus
E_d	=	energy density, W · h/kg
f_i	=	equivalent performance constants
$\hat{\boldsymbol{g}}$	=	spin, transverse, gimbal axis unit vectors
h	=	circular orbit altitude, km
I_T	=	spacecraft principal-axis inertia, kg · m^2
I_w	=	control moment gyro wheel inertia, kg · m^2
J_i	=	candidate performance index a, b, or c
k_s	=	rotor shape factor
l_{rot}	=	rotor length, m
M	=	attitude control + energy storage mass, kg
m_A	=	component A mass based on parameters B, C
N	=	attitude torque, N · m
N_{vc}	=	number of cluster actuators
P	=	instantaneous peak power, W
P_d	=	power density, W/kg
r	=	generic radius, m
r_i	=	rotor inner radius, m
r_o	=	rotor outer radius, m
T_e	=	on-orbit eclipse duration, s
T_i	=	design point score function a, b, or c
t_f	=	slew maneuver time, s
t_{off}	=	slew dead-band, s
t_{sp}	=	wheel spoke thickness, m
t_{life}	=	spacecraft lifetime, eclipse cycles
V_{bus}	=	spacecraft power bus voltage, V
w	=	scoring function weights
x_{msn}	=	transmission efficiency, %
α_i	=	rotor stress integration constants
β	=	control moment gyro pyramid angle, rad
γ	=	design margin weights
δ	=	gimbal angle, rad
$\dot{\delta}$	=	maximum gimbal rate, rad/s
θ_f	=	slew maneuver angle, rad
λ	=	$(E_\theta/E_r)^{0.5}$
ν_{yx}	=	rotor material Poisson's ratio of contraction in x direction because of tension in y direction
ρ	=	density, kg/m^3
σ	=	rotor stress, N/m^2
χ	=	control moment gyro torque efficiency, %
Ω	=	wheel speed, rad/s or revolutions/minute
$\dot{\Omega}$	=	maximum wheel acceleration, rad/s^2

Subscript

a	=	actual
b	=	baseline (comparison) system
dc	=	Mark II direct current motor
g	=	control moment gyro gimbal axis
i	=	ith actuator
m	=	margin
m_j	=	jth wheel motor
mb	=	magnetic bearing
mkii	=	Mark II control moment gyroscope
oth	=	miscellaneous actuator components
r	=	required
R	=	rotor radial direction
real	=	realistic
rot	=	wheel rotor
s	=	control moment gyro spin axis
sc	=	spacecraft (satellite)
sp	=	spoke
struct	=	structure
t	=	control moment gyro transverse axis
ta	=	total allowable
wh	=	wheel (rotor + shaft + motor)
θ	=	rotor tangential direction

Received 12 May 2006; revision received 30 November 2006; accepted for publication 1 December 2006.

*Graduate Student, Surrey Space Center, School of Electronics and Physical Sciences, University of Surrey; d.richie@surrey.ac.uk. Senior Member AIAA.

†Lecturer, Surrey Space Center, School of Electronics and Physical Sciences, University of Surrey; v.lappas@surrey.ac.uk. Senior Member AIAA.

‡Reader, Surrey Space Center, School of Electronics and Physical Sciences, University of Surrey; p.palmer@surrey.ac.uk. Member AIAA.

I. Introduction

TODAY'S small satellites (less than 500 kg in mass) are increasingly considered for large satellite missions such as precision Earth imaging and Space Radar [1–3]. Difficult hurdles face these small satellites' designers, such as meeting stringent mass,

power, and volume constraints which significantly impact cost. To mitigate costs, the Surrey Space Center, in conjunction with Surrey Satellite Technology, Ltd., regularly uses commercial off-the-shelf components in satellite design [1–4]. Assuming that deleting mass eventually enables a change in launch vehicle class and thus, on average, reduces cost, an obvious method to reduce mass but maintain performance is to combine key satellite functions. For example, a satellite's energy storage (ES) function, usually achieved via rechargeable batteries, can be combined with its pointing system [i.e., the attitude control subsystem (ACS)], forming an energy storage and attitude control system (ESACS) [5]. Such an ESACS typically consists of flywheel-based, three-axis stabilizing, momentum exchange actuators such as reaction wheels (RWs), momentum wheels (MWs), control moment gyroscopes (CMGs), or variable-speed CMGs (VSCMGs) doubling as energy storage devices. RWs provide zero-biased momentum through low spin rates, and thus are unrealistic for energy storage. In contrast, MWs have a momentum bias through nonzero nominal spin rate and thus the ability to store and drain flywheel energy, whereas CMGs operate at fixed flywheel speeds without freedom to store and drain energy. However, the CMG torque amplification property in which a small amount of CMG gimbal motor input torque results in a relatively large slewing torque gives it a distinct advantage over an MW-based system [6]. Fortuitously, as illustrated in Fig. 1, VSCMGs combine these CMG and MW advantages while eliminating well-known CMG gimbal-lock singularities by using the MW mode near singularity, and therefore are the most logical ESACS alternative. This paper presents the underlying principles in combining the energy storage and attitude control subsystems and proposes an optimal-sizing strategy for designing an ESACS using VSCMGs. Then, the method is used to size a synthetic aperture radar (SAR) mission and leads to significant mass savings, longer lifetime, increased slewing agility, robust singularity avoidance, and improved power density as compared with a conventional momentum wheel-actuated ACS plus NiCd-battery energy storage design.

II. Background

Roes was the first to propose flywheel energy storage in satellites in 1961 [7], however, it was not until the early 1970s, when coupling Roes' approach with the attitude control function emerged [8–14], spawning several proposals for an ESACS, primarily for future employment on NASA's International Space Station (ISS). As this technology progressed, designers encountered flywheel rotor material and mechanical bearing/levitation barriers to implementation [15,16]. Likewise, many of these early concepts relied on counter-rotating MW implementations while a handful mentioned CMGs as plausible alternatives. Then, in the 1990s, the development of hybrid cars advanced key flywheel technologies such as composite rotors and magnetic bearings. This sparked renewed interest in ESACS in parallel with ISS advancing development. Key related results included the gyrostat investigation in [17] and simultaneous control design for an ESACS subcategory, an integrated power and attitude control system, using four redundant, non-counter-rotating, momentum wheels in [18]. In parallel to these efforts, Hall gave an excellent literature review for this problem in [19].

Nevertheless, building on the work of Tsiotras et al. [18], Richie et al. [5] showed simultaneous momentum wheel and gimbal control were possible by employing the new momentum exchange device theoretical generalization known as the VSCMG, conceptualized by the combined efforts of Ford and Hall [20,21] and Schaub et al. [22]. The VSCMG development was predicated on the detailed CMG theory offered by Jacot and Liska [23], Margulies and Aubrun [24], Oh and Vadali [25], Wie [26], and several others [27–29]. Following the work of Richie et al. [5] work, Yoon and Tsiotras identified a wheel speed equalization technique for reducing the risk that one VSCMG reaches saturation, effectively increasing a VSCMG-suite's utility [30,31]. Other related work involves Roithmayr's VSCMG-gyrostat generalization to gimballed, counter-rotating wheels including satellite-to-actuator damping torque [32] with direct application to systems with a mixture of counter-rotating MWs and standard CMGs.

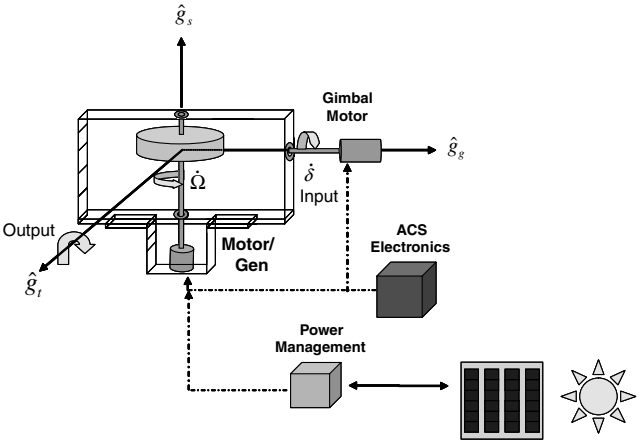

Fig. 1 Variable-speed CMG principles of operation.

Heretofore, the performance of an ESACS was limited due to bearing friction and structural fatigue, hurdles virtually eliminated by composite material and magnetic bearing advances. Without these barriers, two major contemporary ESACS programs targeted for medium to large satellites stand to gain from this technology: NASA's counter-rotating wheels [33–35] and the U.S. Air Force Research Laboratory's VSCMG-like ESCMG work, both focused on laboratory validation before flight. In contrast, small satellite implementation of ESACS VSCMGs has not been done. Only recently has the use of CMGs for large satellites been researched for small satellites [6]. Varatharajoo demonstrated small satellite counter-rotating MW ESACS use [36] and its associated sizing fundamentals. Neither of these efforts, however, address using VSCMGs in an ESACS role nor the associated sizing process or its optimality. For this reason, to advance the current state-of-the-art, an investigation into the optimal design sizing process for a VSCMG cluster in an ESACS is undertaken here, effectively extending the work of Lappas [6] and Varatharajoo [36].

III. Energy Storage and Attitude Control System Fundamentals

A. Process Inputs

The VSCMG-based ESACS physical principles and optimal-sizing process described next rely on reference profiles for attitude and satellite energy storage/power as depicted in Fig. 2. The top three plots show the desired angular acceleration, angular velocity, and angular position of a spacecraft doing a bang–off–bang single-axis maneuver (e.g., roll, pitch, or more generally, a maneuver about the Euler axis), where the starting and stopping torque portions are separated with a dead-band coasting period, and the bottom plot shows a flywheel "battery" power profile where positive values represent power added to the energy storage system for charging, whereas negative values represent power to be drained from it to supply other subsystems (e.g., during eclipse periods). These profiles set two of the key requirements for the ESACS design.

B. Optimal-Sizing Theory

To achieve success, the ESACS engineer needs subsystem design margins (i.e., the differences between the actual design and its associated requirement) that are at or above zero, namely the instantaneous peak power, energy storage capacity, and torque design margins, which drive the designs of the two most prominent ESACS components, the power and attitude control subsystems, and the mass margin M_m due to its importance to cost-effective satellite designs. These margins are defined as

$$N_m = N_a - N_r \tag{1}$$

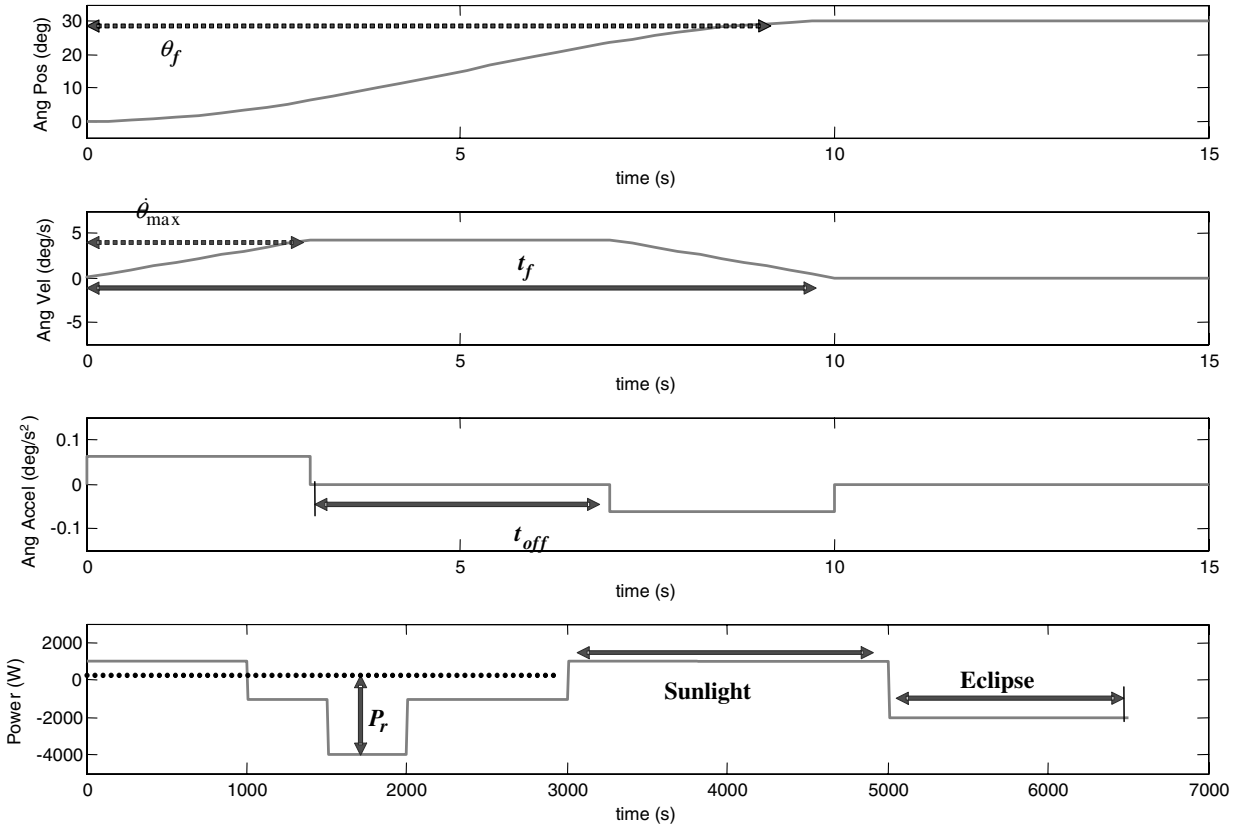

Fig. 2 Bang–off–bang attitude reference maneuver and power profile.

$$P_m = P_a - P_r = N_{\text{vc}} P_{a_1} - P_r \tag{2}$$

$$C_m = C_a - C_r = N_{\text{vc}} C_{a_1} - C_r \tag{3}$$

$$M_m = M_r - M_a = M_r - N_{\text{vc}} M_{a_{1_i}} \tag{4}$$

where in the case of N_m, P_m, and C_m, logically require the actual value to be greater than its requirement to ensure the requirement is met. On the other hand, M_m involves a given budget (i.e., requirement) M_r, in which the actual mass must be less than or equal to M_r. Also, in the case of using a VSCMG cluster for ESACS, the number of actuators is important to capturing the actual storage capacity and peak power (more identical flywheels means more storage capacity and more instantaneous peak power are available) and for obvious reasons, the actual mass of the system. Next, P_r and M_r are directly given by mission requirements, however, N_r is found from the desired maneuver (assumed to be the bang–off–bang maneuver mentioned earlier) as

$$N_r = \frac{4 I_{T_{\max}} \theta_f}{\left(t_f^2 - t_{\text{off}}^2\right)} \tag{5}$$

and the required storage capacity is found from P_r and other mission requirements such as eclipse duration, eclipse duty cycle, flywheel battery depth of discharge (dod), and transmission efficiency as defined in [37]

$$C_r = \frac{d_{\text{ty}} T_e P_r}{\text{dod} x_{\text{msn}}} \tag{6}$$

Knowing the requirements, the actual values are computed next to find the design margins. First, the cluster peak torque N_a, discussed in [38], relies on the torque efficiency of the cluster, the configuration (assumed to be a pyramid configuration as will be addressed later), wheel spin-axis inertia (because it is the largest inertia for each VSCMG), the minimum wheel speed (N_a must be producible at all wheel speeds in each VSCMG's envelope, where the wheels only spin in one direction from minimum speed to maximum speed), and the maximum gimbal rate, in other words,

$$N_a = \chi I_{w_s} \Omega_{\min} \dot{\delta} (2 + 2\cos\beta) \tag{7}$$

Second, the actual power comes from differentiating the wheel spin-axis kinetic energy, $0.5 I_{\text{ws}} \Omega^2$ for each VSCMG, using the maximum power (wheels spinning at maximum speed) but subtracting the unusable power (power produced below the minimum wheel speed)

$$P_{a_1} = I_{w_s} (\Omega_{\max} - \Omega_{\min}) \dot{\Omega} \tag{8}$$

Similarly, the storage capacity in the wheels was best defined by Varatharajoo in [36]

$$C_{a_1} = k_s \sigma_\theta \pi l_{\text{rot}} \left(r_o^2 - r_i^2\right) [1 - (\Omega_{\min}/\Omega_{\max})^2]/3600 \tag{9}$$

Finally, the actual ESACS mass follows from the design approach used, but can typically be described as a sum of the incorporated components. Three different examples of this mass computation are given later in this paper, but each defines $I_{w_s} = 0.5\pi\rho_{\text{rot}} l_{\text{rot}} (r_o^4 - r_i^4)$. Furthermore, Eqs. (1–3) ensure the actual values are greater than or equal to the required values when the design margins are nonnegative. A feasible and practical design is thus defined as one in which the design margins are nonnegative and the relevant constraints are met. Only feasible designs are considered.

Next, six variables drive the design margins and are thus interrelated: $\Omega_{\max}$, $\Omega_{\min}$, l_{rot}, $\dot{\Omega}$, $\dot{\delta}$, and $\sigma_\theta/\rho_{\text{rot}}$. Selecting these decision variables via an optimal-sizing algorithm is addressed next. Furthermore, these parameters are constrained in that $\Omega_{\max}$, $\Omega_{\min}$, l_{rot}, $\dot{\Omega}$, $\dot{\delta}$, $\sigma_\theta/\rho_{\text{rot}}$, plus N_m, P_m, C_m, and M_m must be nonnegative for design feasibility. Added to this, $\Omega_{\max}$ is structurally limited by the flywheel rotor strength, $\Omega_{\min}$ is limited in ensuring enough torque and power is produced by the flywheel, and the disparity between the

maximum and minimum allowable wheel speeds is limited to ensure proper energy is stored. Thus, these constraints drive the feasible selection of these six ESACS design variables.

C. Optimization Logic

Designing effective ESACS VSCMGs centers on selecting the best decision variable combination that optimizes a suitable performance index to meet mission requirements subject to the aforementioned constraints. Because an underlying aim in this task is to produce a system that outperforms the baseline MW ACS plus NiCd ES, three different candidate performance indices, J_a, J_b, and J_c, were crafted to capture the relationship of the ESACS design compared with the baseline. First, J_a is defined as the weighted ratio of the four VSCMG design margins to their baseline counterparts

$$J_a = \frac{\gamma_{a_1} C_m \gamma_{a_2} P_m \gamma_{a_3} N_m \gamma_{a_4} M_{m_i}}{C_{m_b} P_{m_b} N_{m_b} M_{m_b}} = \frac{N_{\text{vc}}^3 \gamma_{a_1} \gamma_{a_2} \gamma_{a_3} \gamma_{a_4} C_{m_1} P_{m_1} N_m M_{m_{i1}}}{C_{m_b} P_{m_b} N_{m_b} M_{m_b}} \tag{10}$$

where the index $i = 1$, 2, or 3 relates to the candidate alternative in consideration (i.e., #1, #2, or #3) and its differently calculated mass. The capacity and power margins are calculated using equations applicable to a single VSCMG and then multiplied by N_{vc} as is the mass margin, but the torque margin (as are the baseline margins) is calculated for the entire VSCMG suite. This has been included in finding J. Regardless, J_b is based on summing the square of the design margins as in

$$J_b = \frac{1}{4}\left[\gamma_{b_1}\left(\frac{N_{\text{vc}} C_{m_1}}{C_{m_b}}\right)^2 + \gamma_{b_2}\left(\frac{N_{\text{vc}} P_{m_1}}{P_{m_b}}\right)^2 + \gamma_{b_3}\left(\frac{N_m}{N_{m_b}}\right)^2 + \gamma_{b_4}\left(\frac{N_{\text{vc}} M_{m_{i1}}}{M_{m_b}}\right)^2\right] \tag{11}$$

and, for J_c, an experimental error approach is taken in regard to the difference between each design margin and its baseline, as in

$$J_c = \frac{1}{4}\left[\gamma_{c_1}\left(\frac{N_{\text{vc}} C_{m_1} - C_{m_b}}{C_{m_b}}\right) + \gamma_{c_2}\left(\frac{N_{\text{vc}} P_{m_1} - P_{m_b}}{P_{m_b}}\right) + \gamma_{c_3}\left(\frac{N_m - N_{m_b}}{N_{m_b}}\right) + \gamma_{c_4}\left(\frac{N_{\text{vc}} M_{m_{i1}} - M_{m_b}}{M_{m_b}}\right)\right] \tag{12}$$

Furthermore, for the best ESACS to baseline ratio one needs to maximize J_i, or equivalently, minimize $J = -J_i$. Incorporating the constraints, one can cast the problem as a standard nonlinear programming problem (NLP) using $J = -J_a$ (or similarly, J_b or J_c).

Minimize

$$J = -\frac{N_{\text{vc}}^3 C_{m_1} P_{m_1} N_m M_{m_{i1}}}{C_{m_b} P_{m_b} N_{m_b} M_{m_b}}, \qquad i = 1, 2, 3 \tag{13}$$

subject to

$$C_{m_1}, P_{m_1}, N_m, M_{m_{i1}} \geq 0 \qquad i = 1, 2, 3 \tag{14}$$

$$\Omega_{\max}, \Omega_{\min}, l_{\text{rot}}, \dot{\Omega} \geq 0 \tag{15}$$

$$\left(\Omega_{\max}^2 - \Omega_{\min}^2\right) l_{\text{rot}} \geq \frac{4 T_e P_r}{N_{\text{vc}} \pi \rho_{\text{rot}} \left(r_o^4 - r_i^4\right)} \tag{16}$$

$$\Omega_{\max} \leq \Omega_{\text{struct}} \tag{17}$$

$$l_{\text{rot}} \leq l_{\text{real}} \tag{18}$$

$$\dot{\Omega} \leq \dot{\Omega}_{\text{real}} \tag{19}$$

$$J \leq -1.0 \tag{20}$$

where Ω_{struct} follows from applying the radial force equilibrium equations defined by Danfelt et al. and addressed in Varatharajoo [36,39] for a typical, anisotropic (orthotropic), single-layer rotor. Captured directly from [36,39], the governing stress equations for a constant speed flywheel are

$$\sigma_r = \alpha_1 \frac{E_r(\lambda + \nu_{\theta r})}{(1 - \nu_{\theta r}\nu_{r\theta})} r^{\lambda - 1} + \alpha_2 \frac{E_r(\nu_{\theta r} - \lambda)}{(1 - \nu_{\theta r}\nu_{r\theta})} r^{-\lambda - 1} - \frac{(3 + \nu_{\theta r})\rho\Omega^2}{9E_r - E_\theta} r^2 \tag{21}$$

$$\sigma_\theta = \alpha_1 \frac{E_\theta(1 + \lambda\nu_{r\theta})}{(1 - \nu_{\theta r}\nu_{r\theta})} r^{\lambda - 1} + \alpha_2 \frac{E_\theta(1 - \lambda\nu_{r\theta})}{(1 - \nu_{\theta r}\nu_{r\theta})} r^{-\lambda - 1} - \frac{(1 + 3\nu_{r\theta})E_\theta\rho\Omega^2}{9E_r - E_\theta} r^2 \tag{22}$$

The integration constants α_1, α_2 are found by applying radial stress boundary conditions (i.e., $\sigma_r = 0$ at $r = r_o$ and $\sigma_r = -t_{\text{sp}}\rho_{\text{sp}}\Omega^2 r_i^2$ at $r = r_i$). Substituting these two values in Eqs. (21) and (22), one can calculate the stress distribution in the wheel for a given wheel speed, or conversely, use the maximum allowable rotor stress to define the maximum allowable wheel speed. The latter of these techniques yields Ω_{struct}. The stress distribution can be viewed graphically in Fig. 3 which directly follows from [36,39]. In these plots, the allowable stress (tensile and compressive) values are superimposed upon the stress distribution plots for determining the maximum allowable structural wheel speed.

Next, the NLP from Eqs. (13) and (14) is solved using a reduced-order gradient method based on crafting a Hamiltonian from the performance index supplemented by a linear combination of the constraints. As applied here, this approach was implemented using the author's Microsoft Excel solver-based sizing tool. Functionality of this iterative process is shown in Fig. 4. The process involves defining mission and actuator parameters, selecting design inputs based on engineering judgement such as design alternative number, optimization type (maximize, minimize, or set to a specific value), and optimization parameter (performance index J or mass M_m), running the optimizer software tool, and interpreting the decision variable outputs for different combinations of $\sigma_\theta/\rho_{\text{rot}}$ (i.e., rotor material parameters). On a basic level, the optimizer software performs the standard parametric design optimization through systematically perturbing the system's parameters to find the best performance index value, but it also uses an iterative reduced-order gradient algorithm designed to reduce the number of computations required for multiple-decision variable problems with hundreds of decision variables as well as a robust error checking code to trap user input errors. Here, the optimizer function generates a single point design (i.e., a specific combination of decision variables) for the given process inputs, another software function generates different variable input combinations such that the entire process produces multiple feasible point designs through several individual optimization iterations in batch mode. The resulting collection of design points is then reviewed, scored, and evaluated in selecting a design. This is further illustrated with a practical example in the next section.

IV. Practical Example

Next, we apply this process to the case of sizing VSCMGs for a small satellite spotlight synthetic aperture radar mission. This type of mission requires agile slewing simultaneously with high instantaneous peak power demand. Table 1 reflects these realistic requirements for such a system. Notice the agile slew maneuver parameters θ_f, t_f, and t_{off} and high peak power demand P_r.

To apply the optimal-sizing process to the given mission requirements, we next identify a few competing candidate design approach alternatives based on the trade tree of key technologies

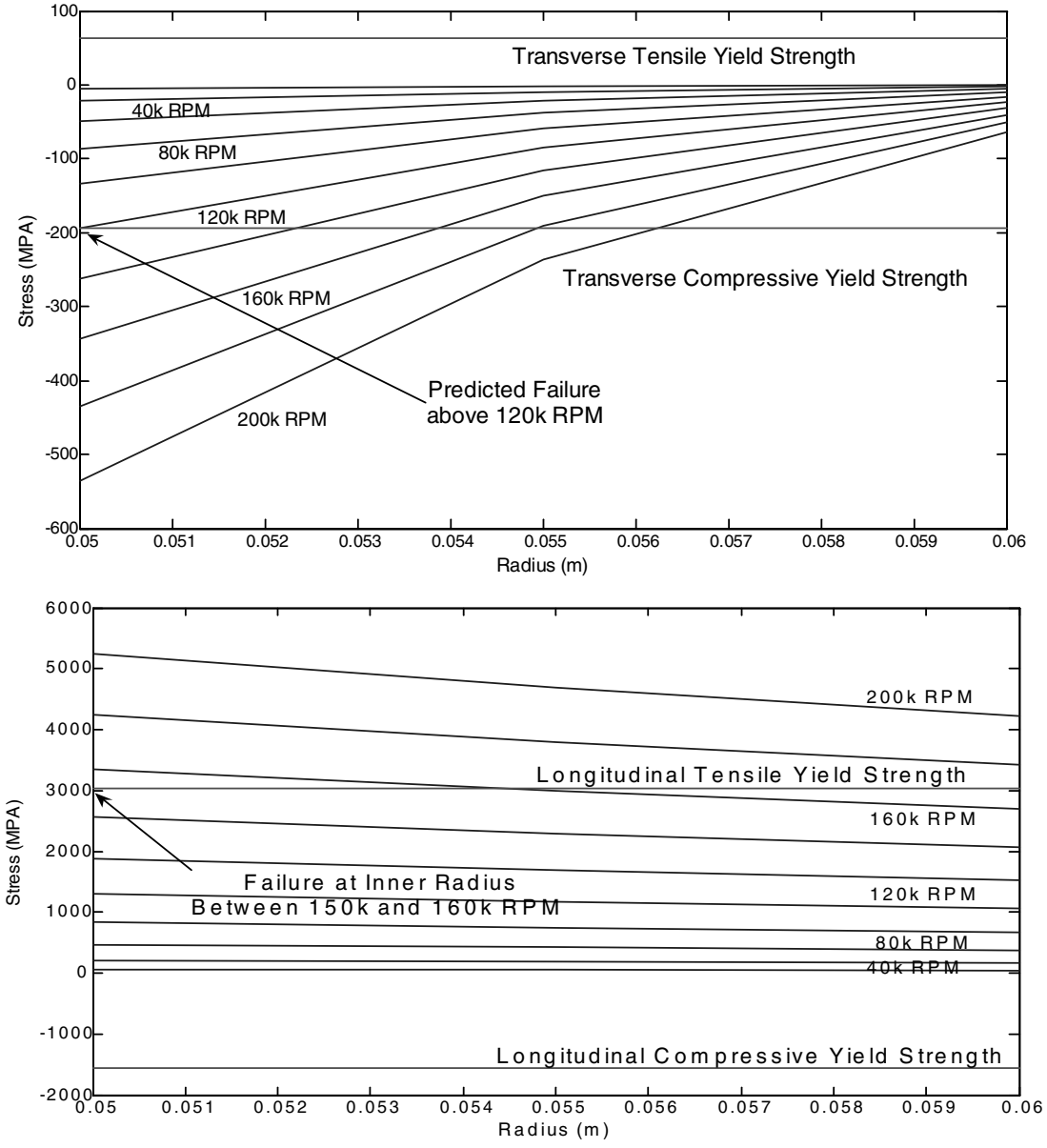

Fig. 3 T1000G carbon fiber radial and tangential stress distributions.

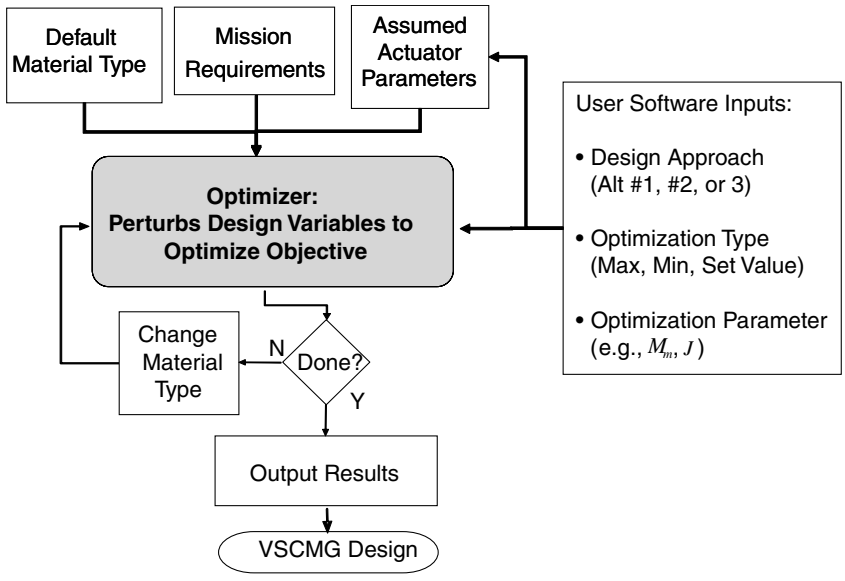

Fig. 4 Basic optimal-sizing process.

Table 1 Space radar requirements

Parameter	Value
Orbit Altitude, h, km	450
Depth-of-discharge, dod, %	80
Transmission efficiency, x_{msn}, %	90
Peak power demand, P_r, W	1100
Eclipse duty cycle, d_{ty}, %	25
Power bus voltage, V_{bus}, V	28
Max single-axis inertia, $I_{T_{\max}}$, kg · m^2	120
Slew maneuver angle, θ_f, deg	140
Slew maneuver time, t_f, s	70
Slew maneuver dead-band, t_{off}, s	12
Satellite total mass, M_{sc}, kg	400
Allowable satellite mass, M_{ta}, kg	450
Allowable ACS plus ES mass, M_r, kg	45

found in Fig. 5. For the purposes of this paper, this rather wide trade space has been narrowed down to three design alternatives by practical pruning of the trade tree. These designs are alternative 1 which uses a cluster of mechanically levitated, gimballed flywheels, based on a conventional design approach like that shown in [40]; alternative 2 which uses an open motor/generator with a magnetically levitated, mechanically gimballed flywheel; and alternative 3 which uses a magnetically levitated, mechanically gimballed flywheel with embedded electromagnets in the rotor for motor/generator functionality like Varatharajoo's nongimballed flywheel shown in [36]. Next, these alternative definitions lead to three different mass (M_a) calculations by summing the appropriate subcomponents:

$$M_{a_{1_1}} = m_{\text{rot}}(l_{\text{rot}}) + m_{\text{oth}}(l_{\text{rot}}) + m_{\text{kii}_{\text{scaled}}} + m_{\text{dc}_{\text{scaled}}} \tag{23}$$

$$M_{a_{1_2}} = m_{\text{rot}}(l_{\text{rot}}) + m_{\text{oth}}(l_{\text{rot}}) + m_{\text{mb}}(l_{\text{rot}}) + 2m_{m_2}(l_{\text{rot}}) \tag{24}$$

$$M_{a_{1_3}} = m_{\text{rot}}(l_{\text{rot}}) + m_{\text{oth}}(l_{\text{rot}}) + m_{\text{mb}}(l_{\text{rot}})m_{m_3}(l_{\text{rot}}, \Omega_{\max}) \tag{25}$$

Directly impacting one of the four key design margins, the functions have an important role in the optimal-sizing process, thus the better one can define them ahead of time, the more accurate the results.

A. Assumptions

Before examining the results from this example, it is important to identify some assumptions made. First, although it has not been included here, rotor containment to prevent personnel and/or systems damage in the event of catastrophic wheel failure is very important, but the larger the containment method used, the greater the mass impact. It is expected that system designers consider this fact when designing a VSCMG-based ESACS for any satellite class. Second, there are several different schemes for initial system startup once the satellite is deployed. This study has not ventured to explore all of these, but awareness of this issue is paramount to future on-orbit success. Plausible methods could include flywheel battery trickle charging, solar panel to super capacitor to VSCMG ESACS charging, or employment of a small primary battery to handle the power load until the VSCMGs are adequately charged to commence on-orbit operation. Third, due to its built-in redundancy and prevalence in the existing literature [6,25,26,41], it is assumed that a pyramid cluster of VSCMGs is to be used in ESACS. This configuration permits all four gimbals to fail while maintaining the ability to recover three axes of attitude control using the remaining wheels in MW mode and still keep enough redundancy for energy storage. However, it is recognized that there are several different plausible cluster configurations [26]. The key effect is that a different configuration will change the N_{vc} used, as well as change the geometry-based $2 + 2\cos\beta$ term in the N_a equation. Fourth, this technology only applies for missions with simultaneous high-precision pointing and high peak power requirements. If either requirement is eliminated, this approach loses its utility. Fifth, the volume is constrained in the sense that outer and inner flywheel rotor radii are fixed where the rotor length can vary between point designs up to a realistic limit. Finally, the presented arguments focus on this technology's role in fulfilling the entire energy storage mission for a satellite, however, an equally plausible alternative is to employ VSCMG ESACS on missions wherein a high-power, high-agility payload only needs the high-power properties of the ESACS during some operations, but the satellite does not need them all the time to run satellite support subsystems. Thus, a contemporary satellite ES can supply eclipse subsystem power using conventional batteries but

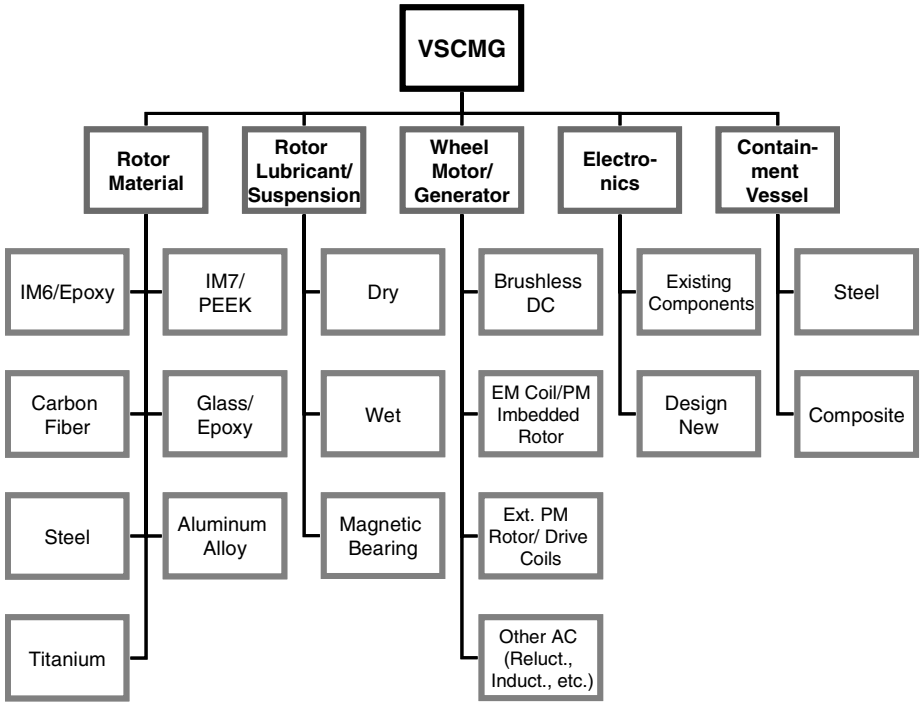

Fig. 5 Key variable-speed CMG technologies.

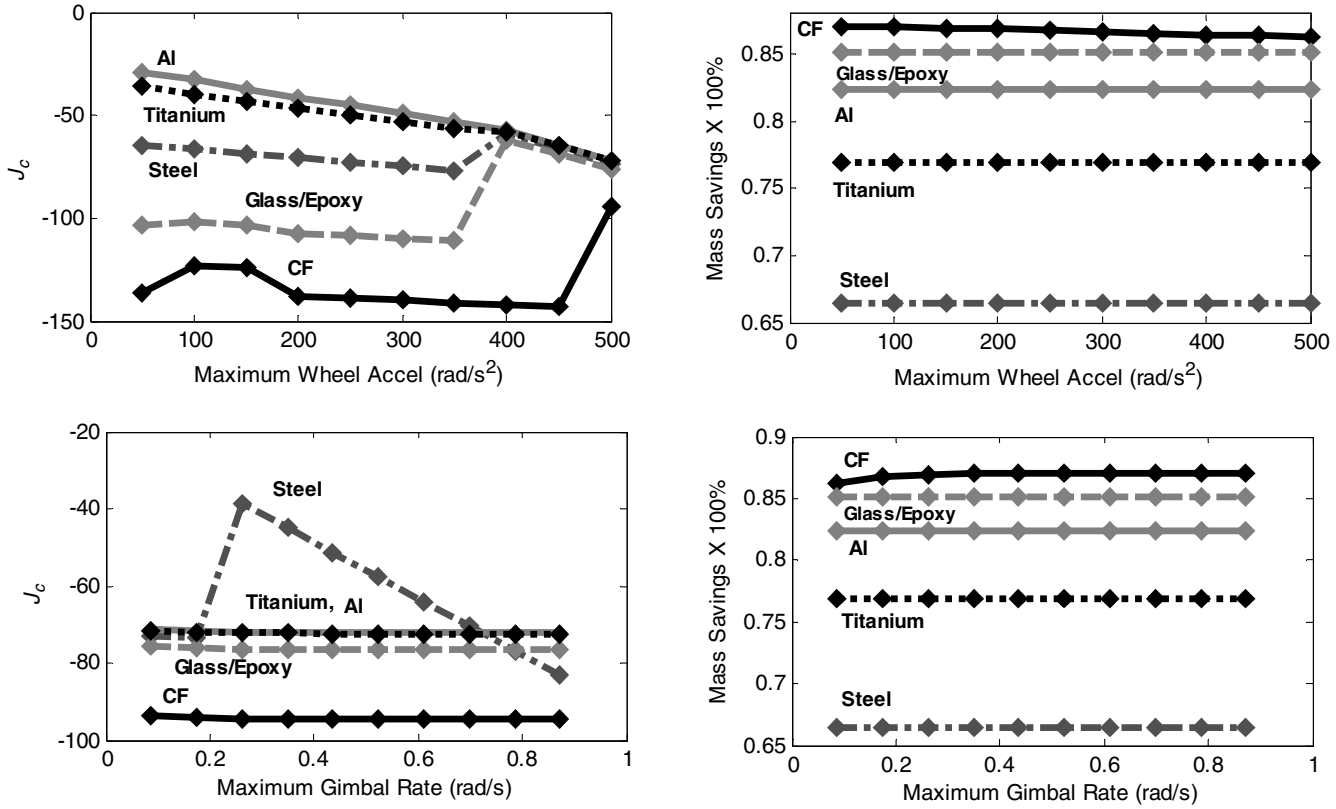

Fig. 6 Optimal performance/optimal mass results for selected rotor materials.

run the payload at the high-power level with energy from the VSCMG ESACS.

B. Sizing Results

Several iterations of the sizing process were run with different variations in the decision variables generating more than 5000 point designs. Selected results reflecting trends in these point designs are shown next. We note here that there are two prominent strategies in completing a design sizing comparison of this nature: sizing for optimal (minimum) mass at a performance equivalent to the baseline system (where "performance" in this sense refers to the nonmass margins, i.e., N_m, P_m, and C_m), or sizing for optimal (maximum) performance at a mass equivalent to the baseline (i.e., $M_m = M_{m_b}$). The former of these often arises when the designer strives to do a similar mission to the baseline but at less mass, whereas the latter arises when the designer attempts to extend the system's capability with the same mass as the old system. Nevertheless, both cases add equality constraints to the NLP.

The first trend investigated is that of different rotor materials. In Fig. 6, the material types have been plotted in terms of wheel acceleration and gimbal rate vs optimal J_c and mass savings. As one can see, the composite materials outperform conventional ones due to more favorable strength to density ratios, $\sigma_\theta/\rho_{\text{rot}}$. Logically, the material with the greatest $\sigma_\theta/\rho_{\text{rot}}$, T1000G carbon fiber, yields the greatest mass savings.

The next trend considered is that of performance index from the choices presented earlier. Figure 7 demonstrates these performance index trends in terms of rotor length. The plots on the left side show the optimal performance indices for different maximum gimbal rate values, whereas those on the right show the performance indices at optimal mass for different maximum wheel acceleration values. Notice that better performance is more negative in value. In both cases, a higher value maximum gimbal rate or maximum wheel acceleration means a better (more negative) performance index, whether using J_a, J_b, or J_c. Also notice that there is a sizable shift in J at a rotor length of approximately 0.035 m in the optimal mass cases. This isolates a good rotor length on which to focus one's design. It should also be noted that each curve is composed of a finite number of design points (10 for each of the cases presented in this report), thus a point on a curve can be thought of as a specific optimized design. Furthermore, J_c yields the best comparison to the baseline. Recall that J_c is defined by the percentage difference between the current design and the baseline where a better point design is a negative value and a better baseline is a positive value. These values, for the case of direct comparisons (as are done in the optimal mass savings case), when multiplied by -100%, give the percent improvement over the baseline. Both figures show a clear transition from positive (better baseline) to negative (better point design) as the rotor length is increased. On the other hand, similar information is harder to glean from the J_b and J_a plots where the performance indices become more negative as rotor length increases, but a percentage improvement as well as the transition from a better baseline to better point design is harder to decipher. Because of its comparative advantages over J_a and J_b, performance index J_c will be used for further plots.

Another very interesting trend is shown in Fig. 8, in which mass savings for alternative 3 is plotted against rotor length. This result illustrates that decreased rotor length is strongly related to improved mass savings.

Next, trends in the decision variables under various conditions are examined. Figure 9 shows trends in wheel speed as compared with the other decision variables and Fig. 10 highlights other relationships between the decision variables. One can see from the wheel speed plots that in design for optimal J, maximum gimbal rate has little to no effect on the wheel speed limits, whereas maximum wheel acceleration has a profound effect on the result. In the latter case, the maximum wheel speed of alternative 3 is significantly less than the others. As for mass savings (MS), a similar wheel speed trend occurs with increased $\dot{\Omega}$ where one will notice that very high maximum wheel speeds are required for lower $\dot{\Omega}$ (i.e., those less than about 100 rad/s^2). However, higher maximum gimbal rates counter-intuitively increase the required maximum wheel speed, but this comes from trying to constrain the nonmass margin design margins (i.e., for equivalent performance) and improve mass savings as much as possible. Also, in the optimal mass savings plots, one can see a

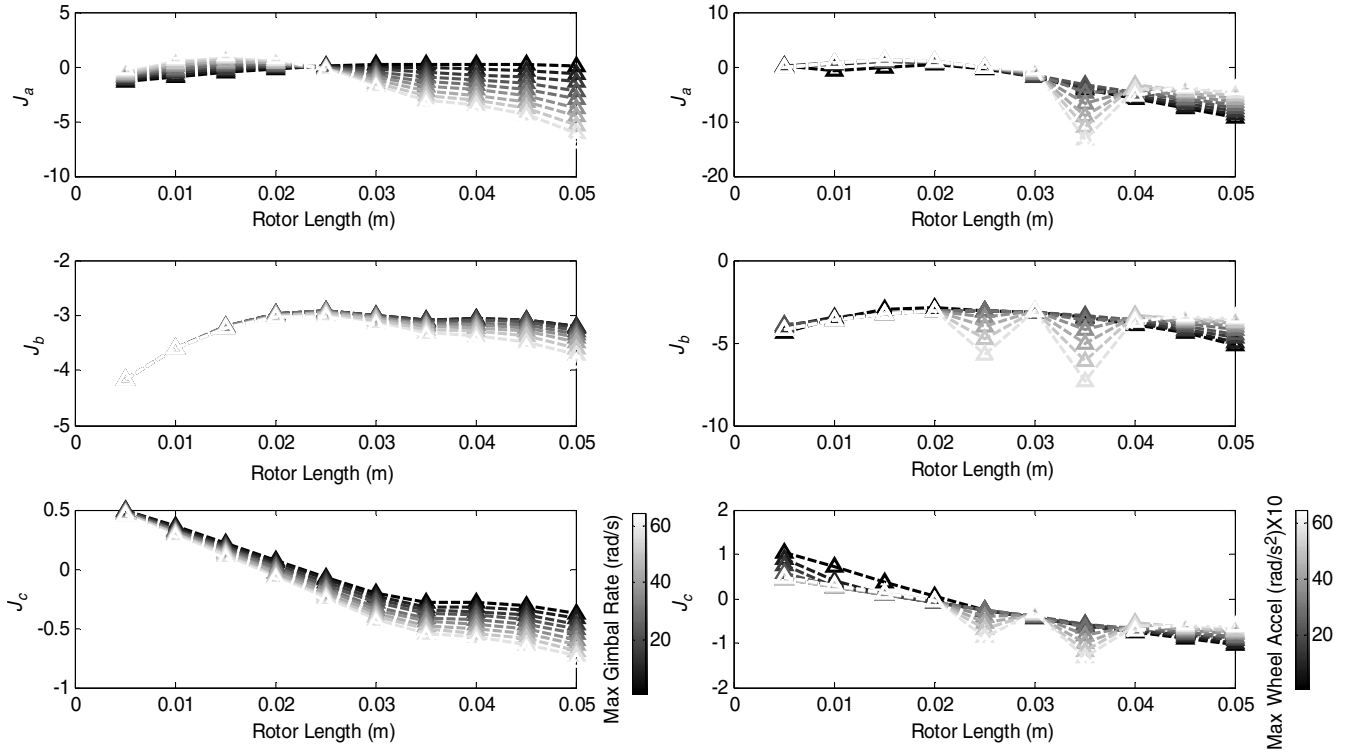

Fig. 7 Rotor length vs performance indices J_a, J_b, and J_c for three alternatives at optimal performance and optimal mass.

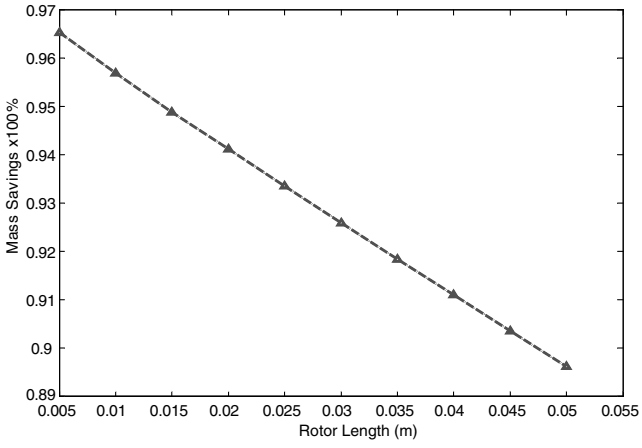

Fig. 8 Rotor length vs optimal mass savings.

large decrease in maximum wheel speed at a rotor length near 0.035 m. Because rotor length affects all of the design margins, this is clearly a rotor length where the margins best match. Continuing on to Fig. 10, one can see the trends in increasing maximum gimbal rate which decreases the required maximum wheel acceleration as well as the rotor length for optimal mass savings. This plot directly illustrates the benefit of torque amplification; increasing the maximum gimbal rate enables decreasing the maximum wheel acceleration in producing equivalent torque while keeping $N_m = N_{m_b}$, $C_m = C_{m_b}$, and $P_m = P_{m_b}$. This change then accounts for the slight decrease in mass savings with increased maximum gimbal rate (similarly maximum wheel acceleration) as the rotor length is also increasing, however, this trend (which is for alternative 1) is inverted for optimal J using alternative 3 (the bottom plot). However, because alternative 3 allows for changes in wheel speed and rotor length when determining motor/generator mass, a key difference in the two parts of Fig. 10 besides optimal MS vs optimal J is that the $\dot{\Omega}$ curves actually intersect.

Next, Fig. 11 shows the relationship between maximum wheel acceleration and rotor length, the energy density and the power density at optimal MS and optimal J. In the case of optimal mass savings, as rotor length increases, energy density increases, until the critical 0.035 m point, then it decreases with increases in rotor length. This is directly correlated to the dominance of the equality-constrained capacity margin (set equal to the baseline capacity margin) until the critical rotor length, after which the mass dominates the energy density calculation (which is simply the actual capacity divided by the subsystem mass). One can also see the main difference in the three technologies at optimal MS in terms of $\Omega_{\max}$ vs E_d and P_d, with alternative 3 showing a significant advantage over the other two technologies. At optimal J, one can see that higher maximum wheel accelerations yield higher energy and power densities. In fact, alternative 1 substantially increases in power and energy density after 450 rad/s^2.

C. Benefits and Scored Designs

The benefits of this approach are significant mass savings, longer lifetime, increased slewing agility, robust singularity avoidance, and improved power density as compared with the baseline. First, faster slewing agility comes from the torque amplification advantage of the actuators' CMG mode as alluded to earlier. Second, mass savings, measured in terms of percent difference between the ESACS subsystem mass and the NiCd secondary battery energy storage system, plus the MW portion of the attitude control system. Note that forecasted ESACS mass improvements have been listed anywhere from 5–15% up to 40–50% and beyond in the literature [32,42], however, the key difference comes from measuring mass savings in terms of direct mass change in the overall spacecraft mass (of which the energy storage plus attitude control subsystems comprise about 10–20% of the total mass) or in terms of the actual subsystem mass percent difference (often well over 50% from combining subsystems). This mass advantage, reflected in the mass comparison before and after combining the systems into a consolidated ESACS using the method defined here as shown in Fig. 12, is one of the primary advantages of implementing this type of system. Third, robust singularity avoidance is reflected in the well-known CMG saturation singularity surface (top plot of Fig. 13) and compared with the VSCMG saturation singularity surface (bottom plot of Fig. 13). Notice that the singular regions (voids) of the CMG momentum

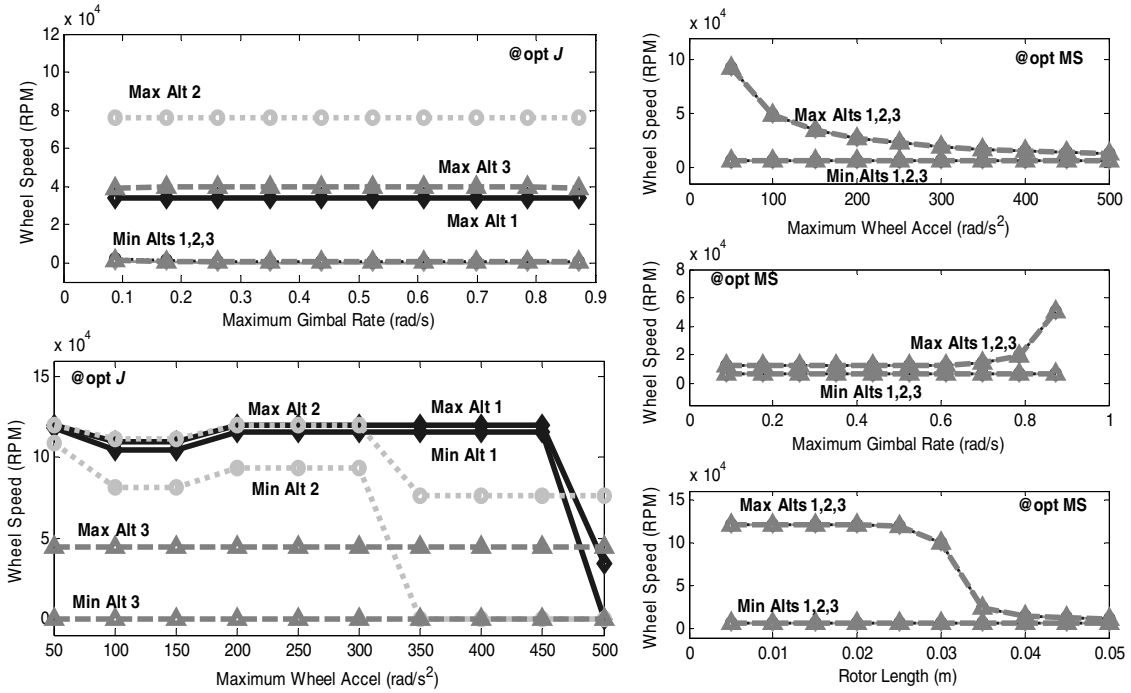

Fig. 9 Maximum and minimum wheel speed comparisons with other decision variables for three alternatives at optimal performance (two plots at left) and optimal mass (three plots at right).

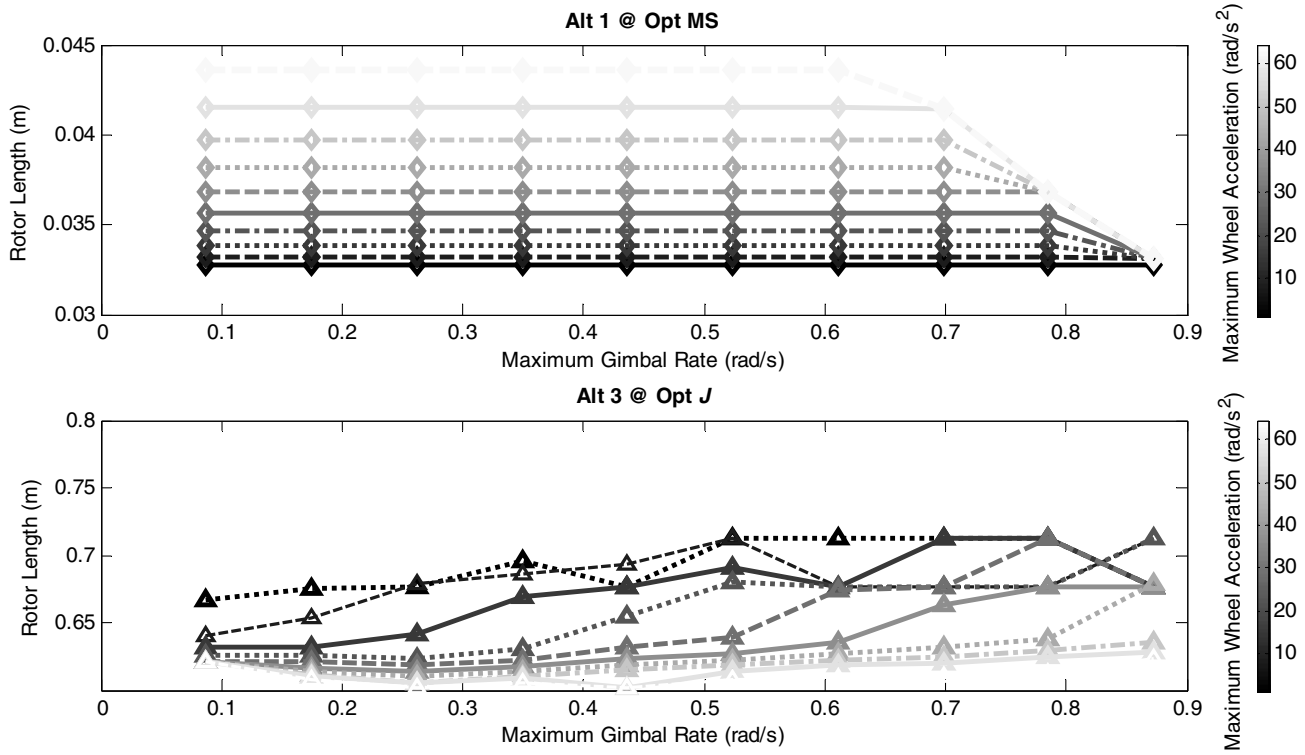

Fig. 10 Maximum gimbal rate vs rotor length comparisons by maximum wheel acceleration for alternatives 1 and 3 at optimal mass savings.

envelope are filled in the case of VSCMGs because the VSCMGs change mode to act as momentum wheels near singularity. Fourth, longer lifetime stems from assuming the best implementation of the VSCMG design comes from magnetic levitation. When enabled, this magnetic levitation permits higher depths of discharge for the flywheel "batteries" as compared with conventional batteries and will return to essentially the same amount of stored energy when topped up after draining them as opposed to conventional batteries which wear out after far fewer cycles. The lifetime argument is best illustrated in Fig. 14, which shows the theoretical position of the flywheel batteries in relation to common secondary battery depths of discharge (dod) vs lifetime. The flywheel depth of discharge has been shown to be limited by the failure time of other onboard subsystems (e.g., solar panels) with an assumed lifetime of 15 years in low Earth orbit. The actual flywheel curve could be much further out in terms of cycles depending upon the performance of the magnetic bearings. As an aside, when reliability details of the ESACS actuator components are known, these reliability factors (which optionally can be thought

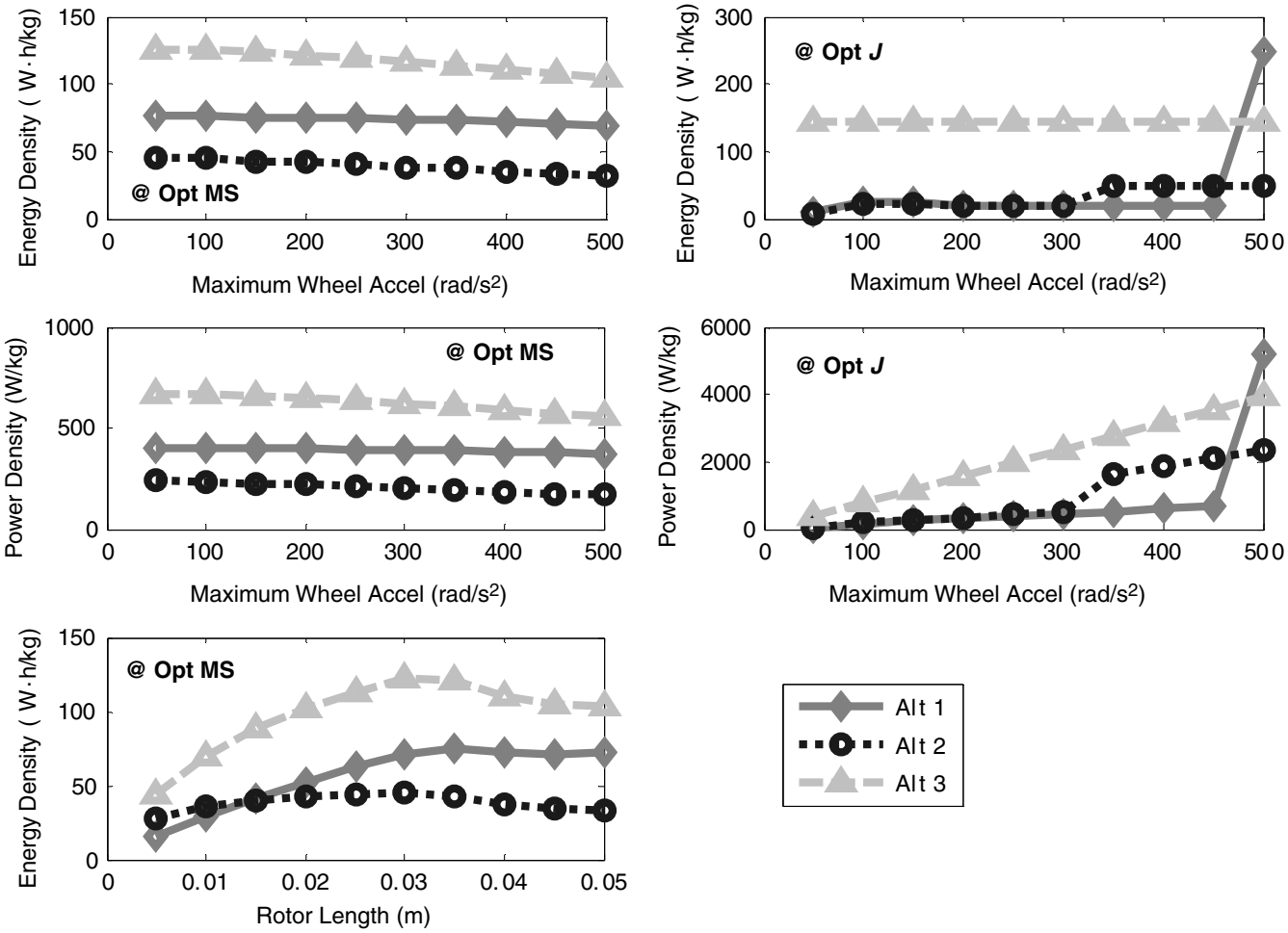

Fig. 11 Selected decision variables vs energy and power density at optimal mass and optimal performance for all three alternatives.

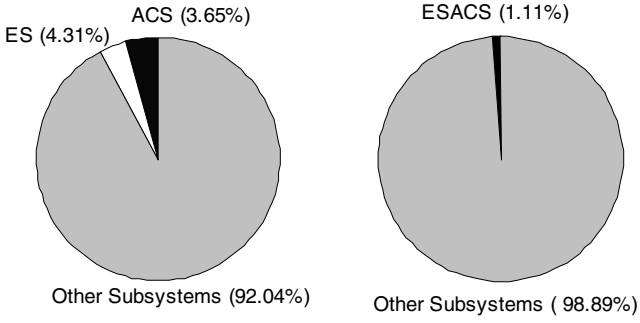

Fig. 12 Spacecraft mass breakdown before and after combining subsystems.

of as a function of decision variables such as maximum/minimum wheel speed, maximum wheel acceleration, etc.) can be used to calculate the lifetime of the system and refine its position in Fig. 14. An example of this would be to calculate the wheel motor/generator's mean time-to-failure as a function of wheel speed, then determine its lifetime in terms of cycles or orbits. This, then, permits refining the VSCMGs place in this chart. In terms of the study shown here, this was actually done for the system used, but it was determined that the lifetime of the first non-ESACS subsystem to fail was less than the motor/generator's lifetime.

The final and perhaps biggest advantage of using an ESACS is reflected in the Ragone plot of Fig. 15, which shows energy density vs power density for the flywheels and the typical secondary

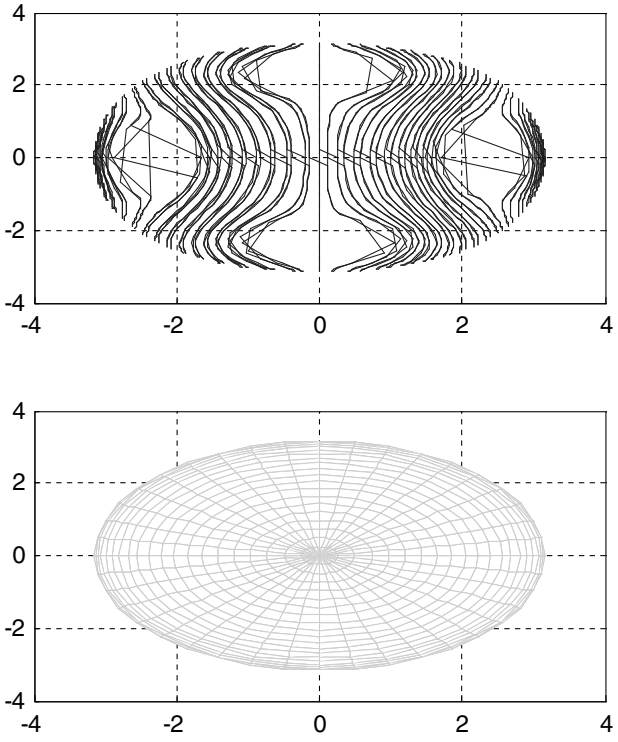

Fig. 13 Pyramid cluster CMG and VSCMG momentum envelopes.

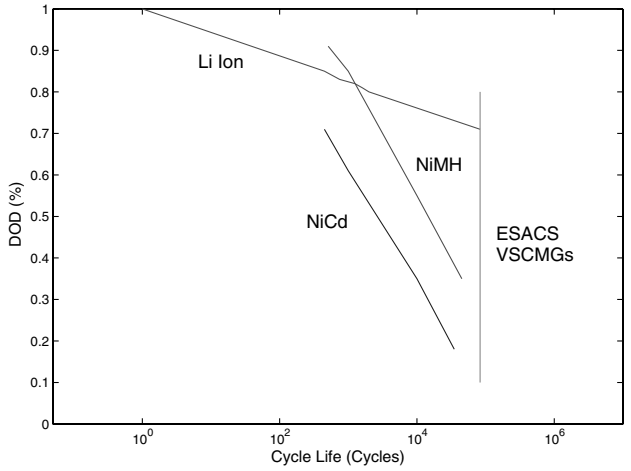

Fig. 14 Depth-of-discharge vs lifetime.

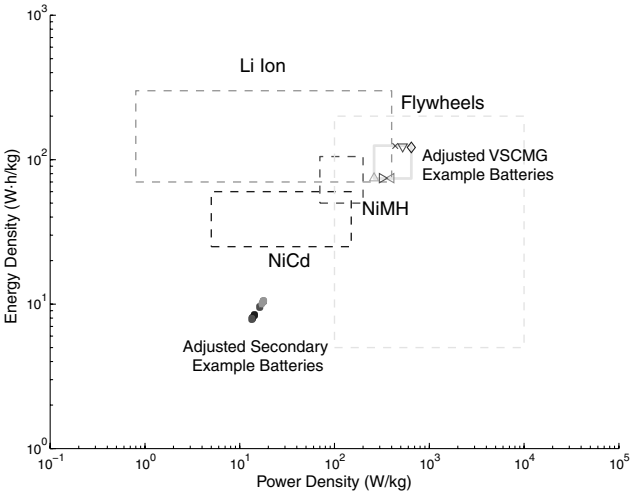

Fig. 15 Adjusted technology Ragone plot, energy density vs power density.

batteries, both of which have been adjusted by mass of the entire energy storage system vs a single battery (as is typically computed). This plot illustrates that even though battery technology is improving (such as lithium-ion) in terms of energy density, flywheels are excellent performers in terms of power density. This is important for small satellites because its primary bus can be designed to handle low peak power requirements using standard secondary batteries and then be supplemented with a VSCMG-based ESACS for high-slewing capability and enjoy the vast improvement in peak power due to the flywheel power density advantage (reflected in the Ragone plot). This is ideal for missions such as Earth imaging and spotlight synthetic aperture radar which have these aggressive peak power and agility requirements. In such a case, a VSCMG system would be an ideal fit combined with a standard small satellite bus.

From the dual-objective sizing process described earlier (i.e., design for maximum mass savings and design for equivalent mass), a table of scored designs was crafted weighting the dual objectives equally. An important note is that the weights can be adjusted based on the designer's preference within the scoring function similar to the design margin weights in the performance index. The scoring function is given for T_a in Eq. (26) which uses J_a (or alternately, T_b and T_c, which use J_b and J_c, respectively), the weights, already mentioned, and normalization factors f_i for equivalent comparisons:

$$\begin{aligned} T_a = {} & \omega_1 f_1 t_{\text{life}} + \omega_2 f_2 E_{d_{\text{MS}}} + \omega_3 f_3 E_{d_{J_a}} + \omega_4 f_4 P_{d_{\text{MS}}} + \omega_5 f_5 P_{d_{J_a}} \\ & + \omega_6 (1 - f_6 \Omega_{\max_{\text{MS}}}) + \omega_7 (1 - f_7 \Omega_{\max_{J_a}}) \\ & + \omega_8 (1 - f_8 \Omega_{\max_{\text{MS}}}) + \omega_9 (1 - f_9 \Omega_{\max_{J_a}}) \\ & + \omega_{10} (1 - f_{10} l_{\text{rot}_{\text{MS}}}) + \omega_{11} (1 - f_{11} l_{\text{rot}_{J_a}}) + \omega_{12} (1 - f_{12} \dot{\delta}_{\text{MS}}) \\ & + \omega_{13} (1 - f_{13} \dot{\delta}_{J_a}) + \omega_{14} (1 - f_{14} \dot{\Omega}_{\text{MS}}) + \omega_{15} (1 - f_{15} \dot{\Omega}_{J_a}) \\ & + \omega_{16} f_{16} MS_{\text{MS}} + \omega_{17} f_{17} J_{a_{J_a}} \end{aligned} \tag{26}$$

Note that this scoring function sums the effects of the benefits (the first five terms), the decision variables (the next 10 terms), the optimization objective (the next two terms), and the technology readiness (the last term). Furthermore, the decision variable quantities are penalized in the scoring function to keep the values as small as permissible (i.e., easier to implement in hardware) given the constraints. Also, the normalization factors are the maximum possible values of each parameter (e.g., 1) the upper bound on a decision variable, or 2) the largest value in the table of point design parameters).

For the purpose of sizing a system to meet the given requirements, several point designs were generated with the different objectives (i.e., optimal mass savings and optimal performance) and scored, weighting the benefits, decision variables, optimization objectives, and technology readiness on an equivalent basis (and the individual terms equally within these groups). In practice, these weights should be tailored to the needs of the designer. Nevertheless, some of the key design points and associated scores are shown in Tables 2–4, relating to results from designing for optimal performance, optimal mass, and a hybrid between the two, respectively, assuming a carbon fiber rotor-based design. Also, the design points were generated using a design-of-experiments, full factorial test matrix approach wherein variation of each decision variable was controlled (either fixed or free) to isolate the relationships between decision variables, benefits, and performance. Only a sample of these variation types (all of which use a carbon fiber rotor and permit l_{rot} and $\Omega_{\max}$ to freely vary) are shown in the tables where the types are defined to be 1) $\dot{\Omega}$ fixed at upper boundary, $\dot{\delta}$ free to vary; 2) $\dot{\Omega}$ free to vary, $\dot{\delta}$ fixed at upper boundary; 3) $\dot{\Omega}$ free to vary, $\dot{\delta}$ fixed at lower boundary; 4) $\dot{\Omega}$ fixed to intermediate boundary, $\dot{\delta}$ fixed at upper boundary; 5) $\dot{\Omega}$ fixed to intermediate boundary, $\dot{\delta}$ fixed at high intermediate boundary; 6) $\dot{\Omega}$ fixed to intermediate boundary, $\dot{\delta}$ free to vary; 7) $\dot{\Omega}$ free to vary, $\dot{\delta}$ fixed at high intermediate boundary; and 8) $\dot{\Omega}$ fixed at upper boundary, $\dot{\delta}$ fixed at upper boundary.

Table 5 summarizes the key parameters for the selected near-term, midterm, and long-term designs from applying this method. The chosen design concept uses a carbon fiber rotor 0.035 m long that is mechanically levitated in the near term and magnetically levitated in the long term with a wheel speed envelope of 6510–50,600 rpm, maximum gimbal rate of 50 deg/s, near- and midterm maximum wheel acceleration of 96 rad/s^2, and long-term maximum wheel acceleration of 500 rad/s^2, resulting in an energy density of 76 W ·

Table 2 Selected optimal *J* results

Alt	J_c	$\Omega_{\min}$	$\Omega_{\max}$	l_{rot}	$\dot{\delta}$	$\dot{\Omega}$	E_d	P_d	Score	Rank	Variation
1	−94.6	50	34,030	0.825	50	500	249	5220	0.452	1 (tie)	1
1	−94.6	50	34,030	0.825	50	500	249	5220	0.452	1 (tie)	2
3	−78.5	990	38,900	0.632	5	500	191	4460	0.392	15	3
3	−78.8	830	39,100	0.624	50	500	189	4450	0.392	16	2
2	−35.4	230	76,200	0.164	50	500	50	2330	0.224	108	1

Table 3 Selected optimal MS results

Alt	MS_c	$\Omega_{\min}$	$\Omega_{\max}$	l_{rot}	$\dot{\delta}$	$\dot{\Omega}$	E_d	P_d	Score	Rank	Variation
3	92.1%	6510	48,950	0.0332	50	100	124	665	0.314	1	4
3	92.1%	6510	48,900	0.0332	45	100	124	665	0.314	3	5
3	92.1%	6510	50,600	0.0332	50	96	125	665	0.314	12	2
1	87.0%	6510	48,900	0.0332	50	100	76	403	0.280	105	6
2	78.0%	6510	48,950	0.0332	50	100	45	238	0.247	241	4

Table 4 Selected composite results using opt MS parameters

Alt	J_c	MS_c	$\Omega_{\min}$–$\Omega_{\max}$	l_{rot}	$\dot{\delta}$	$\dot{\Omega}$	E_d	P_d	Score	Rank	Variation
3	−78.8	92.1%	6510–50,600	0.033	50	96	125	665	0.772	1	2
3	−78.0	91.6%	6510–19,200	0.037	45	301	116	622	0.757	2	7
3	−78.8	92.1%	6510–15,000	0.033	50	500	103	665	0.745	3	8
1	−94.6	87.0%	6510–50,600	0.033	50	96	76	403	0.731	16	2
2	−35.4	78.0%	6510–50,600	0.033	50	96	45	238	0.537	129	2

Table 5 Summary of selected designs using presented sizing algorithm

Parameter	Value	Value	Value
Timing	near term	medium term	long term
Alternative	1	3	3
Overall rank	16	1	3
Minimum wheel speed, $\Omega_{\min}$, rpm	6510	6510	6510
Maximum wheel speed, $\Omega_{\max}$, rpm	50,600	50,600	15,000
Rotor length, l_{rot}, m	0.0332	0.0332	0.0332
Maximum gimbal rate, $\dot{\delta}$, deg/s	50	50	50
Maximum wheel acceleration, $\dot{\Omega}$, rad/s^2	96	96	500
Energy density, E_d, W · h/kg	76	125	103
Power density, P_d, W/kg	404	665	665

h/kg and power density of 404 W/kg in the near term evolving to 103 W · h/kg and 665 W/kg in the long term.

V. Conclusions

A compact and novel optimal-sizing algorithm for a small satellite combined energy storage and attitude control subsystem (ESACS) has been developed and applied to a practical synthetic aperture radar mission to compare and contrast technology design alternatives, trade key system/decision variable parameters, and showcase several benefits. Merging the subsystems eliminates redundant secondary battery mass while incorporating advanced technologies such as composite flywheel rotors and magnetic levitation allows higher sustained rotor speeds and further decreases subsystem and total spacecraft mass. Flywheel energy density advantages are on par with improvements in new secondary battery technologies, whereas increased flywheel power densities over mature and burgeoning secondary batteries follows from the ability to rapidly discharge the energy in the flywheel at much faster rates. Employing magnetically levitated flywheels also permits longer subsystem lifetime through more charge/drain cycles at higher depths of discharge than secondary batteries. The employed redundant VSCMG pyramid configuration with flywheel speed variability permits transition to momentum wheel mode to pass through singularities while predominantly using the CMG mode for its torque amplification advantages. Increased slewing agility is a well-documented direct consequence of employing this CMG mode.

In the new sizing/optimization method, a performance index is used to identify trends in decision variables and pinpoint the optimum rotor length for different technology alternatives. Three candidate performance indices were presented and compared leading to selection of the best of these, which uses an experimental error approach, because it best isolates the transition from conventional to VSCMG-based ESACS design utility.

The sizing/optimization algorithm has shown some important design trends for an ESACS besides the subsystem/spacecraft mass savings. Increasing the gimbal rates of the VSCMGs at an optimal mass reduces the required flywheel acceleration therefore enhancing CMG torque amplification and reducing the problem of flywheel lifetime due to very high wheel speeds. Analysis of the performance index shows that at an optimal mass the maximum flywheel acceleration corresponds to an optimal rotor length, which is used to select the optimal ESACS design. When further analyzed for flywheel acceleration against flywheel speed, the data show that the embedded motor magnetic bearing technology alternative is superior to other technologies, but critical flywheel acceleration points were determined in which other motor technologies can have similar performance values. Additional analysis highlights the benefit of using carbon fiber flywheel rotors: the best performance with maximum mass savings. This fact was also used to qualitatively validate the developed algorithm.

By using this approach, one can best optimally size a VSCMG-based ESACS, quickly identify its utility compared to a contemporary system, and pinpoint the key system parameters required to make the design a reality. The leads to a more efficient, yet highly effective subsystem design.

Acknowledgments

The views expressed in this article are those of the authors and do not reflect the official policy or position of the United States Air Force, Department of Defense, or the U.S. Government. This effort was funded under United States Government Grant FA8655-05-1-3037 between the Surrey Space Center at the University of Surrey and the U.S. Air Force's European Office of Advanced Research and Development. The authors would specifically like to thank Barrett Flake from the U.S. Air Force's European Office of Advanced Research and Development, as well as Jerry Fausz and Brian Wilson at the United States Air Force Research Laboratory for their efforts in sponsoring this investigation. Furthermore, the authors appreciate the reviewers' feedback which helped strengthen the paper's quality.

References

[1] Ward, J., Jason, S., and Sweeting, M., "Microsatellite Constellation for Disaster Monitoring," *Proceedings of the 13th Annual AIAA/USU Conference on Small Satellites, Logan, Utah*, AIAA Paper SSC99-V-2, Aug. 1999.

[2] Bradford, A., Gomes, L., and Sweeting, M., "BILSAT-1: a Low-Cost, Agile, Earth Observation Microsatellite for Turkey," *Proceedings of the 53rd International Astronautical Congress, Houston, Texas*, International Astronautical Federation, Paper IAC-02-IAA.11.3.02, Oct. 2002.

[3] Van Der Zel, V., Blewett, M., Clark, C., and Hamill, D., "Three Generations of DC Power Systems for Experimental Small Satellites," *Proceedings of the Applied Power Electronics Conference, San Jose, CA*, Vol. 2, INSPEC, Accession No. 5274384, DOI , March 1996, pp. 664–670.

[4] Ward, J., and Sweeting, M., "First In-Orbit Results from the UOSAT-12 Minisatellite," *Proceedings of the 13th Annual AIAA/USU Conference on Small Satellites, Logan, Utah*, AIAA Paper No. SSC99-1-2, Aug. 1999.

[5] Richie, D., Tsiotras, P., and Fausz, J., "Simultaneous Attitude Control and Energy Storage Using VSCMGs: Theory and Simulation," *Proceedings of the American Control Conference*, Vol. 5, Inst. of Electrical and Electronics Engineers, Piscataway, NJ, 2001, pp. 3973–3979.

[6] Lappas, V., "Control Moment Gyro (CMG) Based Attitude Control System (ACS) for Agile Small Satellites," Ph.D. Dissertation, School of Electronics and Physical Sciences,, Univ. of Surrey, Guildford, England, U.K., Oct. 2002.

[7] Roes, J. B., "Electro-Mechanical Energy Storage System for Space Application," *Progress in Astronautics and Rocketry*, Vol. 3, 1961, pp. 613–622.

[8] Notti, J., Cormack, A., and Klein, W., "Integrated Power/Attitude Control System (IPACS)," *Journal of Spacecraft and Rockets*, Vol. 12, No. 8, 1975, pp. 485–491.

[9] Adams, L., "Application of Isotensoid Flywheels to Spacecraft Energy and Angular Momentum Storage," NASA, TR CR-1971, Astro Research Corp., Santa Barbara, CA, 1972.

[10] Notti, J., "Integrated Power/Attitude Control System (IPACS) Study, Vol. 1: Feasibility Studies," NASA, Rept. CR 2383, April 1974.

[11] Anderson, W., and Keckler, C., "Integrated Power/Attitude Control System (IPACS) for Space Application," *Proceedings of the 5th IFAC Symposium on Automatic Control in Space*, Pergamon, New York, 1973, pp. 81–92.

[12] Cormack, A., III, "Three Axis Flywheel Energy and Control Systems," NASA, TR TN-73-G&C-8, North American Rockwell Corp., 1973.

[13] Will, R., Keckler, C., and Jacobs, K., "Description and Simulation of an Integrated Power and Attitude Control System Concept for Space-Vehicle Application," NASA TR TN-D-7459, 1974.

[14] Notti, J., Schmill, W., Klein, W., and Cormack, A. I., "Integrated Power/Attitude Control System (IPACS) Study, Volume 2: Conceptual Designs," NASA TR CR-2384, Rockwell International Space Div., Downey, CA, 1974.

[15] Kirk, J. A., "Flywheel Energy Storage Part 1: Basic Concepts," *International Journal of Mechanical Sciences*, Vol. 19, No. 4, 1976, pp. 223–231.

[16] Kirk, J. A., and Studer, P., "Flywheel Energy Storage Part 2: Magnetically Suspended Superflywheel," *International Journal of Mechanical Sciences*, Vol. 19, No. 4, 1976, pp. 233–245.

[17] Hall, C., "High-Speed Flywheels for Integrated Energy Storage and Attitude Control," *Proceedings of the American Control Conference, Albuquerque, NM*, American Automatic Control Council, Vol. 3, New York, 1997, pp. 1894–1898.

[18] Tsiotras, P., Shen, H., and Hall, C., "Satellite Attitude Control and Power Tracking with Energy/Momentum Wheels," *Journal of Guidance, Control, and Dynamics*, Vol. 24, No. 1, 2001, pp. 23–34.

[19] Hall, C., "Integrated Spacecraft Power and Attitude Control Systems Using Flywheels," U.S. Air Force Inst. of Technology, Rept. AFIT/ENY/TR-000, Dayton, OH, 2000.

[20] Ford, K. A., and Hall, C. D., "Singular Direction Avoidance Steering for Control-Moment Gyros," *Journal of Guidance, Control, and Dynamics*, Vol. 23, No. 4, 2000, pp. 648–656.

[21] Ford, K. A., "Reorientations of Flexible Spacecraft Using Momentum Exchange Devices," Ph.D. Dissertation, U.S. Air Force Inst. of Technology, Wright-Patterson AFB, OH, Sept. 1997.

[22] Schaub, H., Vadali, S. R., and Junkins, J. L., "Feedback Control Law for Variable Speed Control Moment Gyros," *Journal of the Astronautical Sciences*, Vol. 46, No. 3, 1998, pp. 307–28.

[23] Jacot, A. D., and Liska, D., "Control Moment Gyros in Attitude Control," *Journal of Spacecraft and Rockets*, Vol. 3, No. 9, 1966, pp. 1313–1320.

[24] Margulies, G., and Aubrun, J., "Geometric Theory of Single-Gimbal Control Moment Gyro Systems," *Journal of the Astronautical Sciences*, Vol. 26, No. 2, 1978, pp. 159–191.

[25] Oh, H., and Vadali, S., "Feedback Control and Steering Laws for Spacecraft Using Single Gimbal Control Moment Gyros," *Journal of the Astronautical Sciences*, Vol. 39, No. 2, 1991, pp. 183–203.

[26] Wie, B., *Space Vehicle Dynamics and Control*, AIAA Education Series, AIAA, Reston, VA, 1998, pp. 435–445.

[27] Paradiso, J., "Global Steering of Single Gimballed Control Moment Gyroscopes Using a Directed Search," *Journal of Guidance, Control, and Dynamics*, Vol. 15, No. 5, 1992, pp. 1236–1244.

[28] Bedrossian, N., Paradiso, J., Bergmann, E., and Rowell, D., "Steering Law Design for Redundant Single Gimbal Control Moment Gyroscopes," *Journal of Guidance, Control, and Dynamics*, Vol. 13, No. 6, 1990, pp. 1083–1089.

[29] Bedrossian, N., Paradiso, J., Bergmann, E., and Rowell, D., "Redundant Single Gimbal Control Moment Gyroscope Singularity Analysis," *Journal of Guidance, Control, and Dynamics*, Vol. 13, No. 6, 1990, pp. 1096–1101.

[30] Yoon, H., and Tsiotras, P., "Spacecraft Adaptive Attitude and Power Tracking with Variable Speed Control Moment Gyroscopes," *Journal of Guidance, Control, and Dynamics*, Vol. 25, No. 6, 2002, pp. 1081–1090.

[31] Yoon, H., and Tsiotras, P., "Singularity Analysis of Variable Speed Control Moment Gyros," *Journal of Guidance, Control, and Dynamics*, Vol. 27, No. 3, 2004, pp. 374–386.

[32] Roithmayr, C., Karlgaard, C., Kumar, R., and Bose, D., "Integrated Power and Attitude Control with Spacecraft Flywheels and Control Moment Gyroscopes," *Journal of Guidance, Control, and Dynamics*, Vol. 27, No. 5, 2004, pp. 859–873.

[33] Kenny, B., Kascak, P., Jansen, R., Dever, T., and Santiago, W., "Control of a High Speed Flywheel System for Energy Storage in Space Applications," NASA TM 2004-213356, Nov. 2004.

[34] Kenny, B., Kascak, P., Jansen, R., and Dever, T., "Flywheel Energy Storage System Demonstration for Space Applications," *Proceedings of the International Electric Machines and Drives Conference, Madison, WI*, NASA TM 2003-212346, June 2003.

[35] Kenny, B., Jansen, R., Kascak, P., Dever, T., and Santiago, W., "Demonstration of Single Axis Combined Attitude Control and Energy Storage Using Two Flywheels," *Proceedings of the 2004 IEEE Aerospace Conference, Big Sky, MN, 6–13 March 2004*, Vol. 4, Inst. of Electrical and Electronics Engineers Paper AC1261, 2004; also NASA TM 2004-212935, pp. 2801–2819.

[36] Varatharajoo, R., "Synergisms for Spacecraft Attitude Control System," Ph.D. Thesis, Dresden Technical Univ., Shaker Verlag, Achen, DE, June 2003.

[37] Larson, W., and Wertz, J., *Space Mission Analysis and Design*, 3rd ed., Kluwer Academic, Boston, MA, 2003, pp. 241–297.

[38] Lappas, V., and Wie, B., "CMG Sizing for Minisatellites," Univ. of Surrey, TN 2, Surrey Space Center, Guildford, England, U.K., 2004, for European Space Agency.

[39] Danfelt, E., Hewes, S., and Chou, T., "Optimization of Composite Flywheel Design," *International Journal of Mechanical Sciences*, Vol. 19, No. 2, 1977, pp. 69–78.

[40] Lappas, V., Steyn, W., and Underwood, C., "Design and Testing of a Control Moment Gyroscope Cluster for Small Satellites," *Journal of Spacecraft and Rockets*, Vol. 42, No. 4, 2005, pp. 729–739.

[41] Schaub, H., "Novel Coordinates for Nonlinear Multibody Motion with Applications to Spacecraft Dynamics and Control," Ph.D. Dissertation, Texas A&M Univ., Arlington, TX, May 1998.

[42] Radzykewycz, D., Fausz, J., and James, W., "Energy Storage Technology Development at the Air Force Research Laboratory Space Vehicles Directorate," *Proceedings of the 1999 Space Technology Conference and Exposition, Albuquerque, NM, 28–29 Sept. 1999*, AIAA Paper No. 99-4503Sept. 1999, pp. 1–5.

D. Spencer
Associate Editor